Calomel acousto-optical cell for spectroscopic applications using non-collinear two-phonon light scattering

Technical Report No. 626

Principal contributors:

Alexandre S. Shcherbakov and Adán Omar Arellanes.

National Institute for Astrophysics, Optics, and Electronics (INAOE), Puebla, Mexico.

National Institute for Astrophysics, Optics, and Electronics (INAOE),

Puebla, Mexico.

Department for Optics, INAOE

Index

ABSTRACT.

We study potentials of a new wide-aperture crystalline calomel-made acousto-optical cell. Characterizing this cell is non-trivial due to the chosen regime based on an advanced non-collinear two-phonon light scattering. Recently revealed important features of this phenomenon are essentially exploited in the new cell and investigated in more detail. These features can be observed simpler in tetragonal crystals, e.g. calomel, exhibiting specific acousto-optical nonlinearity caused by the acoustic waves of finite amplitude. This parametric nonlinearity manifests itself at low acoustic powers in calomel possessing linear acoustic attenuation. The formerly identified additional degree of freedom, unique to this regime, is exploited for designing the cell with an eye to doubling the resolution due to two-phonon processes. We clarify the role of varying the central acoustic frequency and acoustic attenuation using that degree of freedom. Then, the efficiency of calomel is exploited to expand the cell's bandwidth at the cost of its efficiency. Proof-of-principle experiments confirm the developed approaches and illustrate their applicability to innovative technique of optical spectrum analysis with the improved resolution. The achieved spectral resolution 0.205 Å at 405 nm and the resolving power 19,800 are the best to our knowledge for acousto-optical spectrometers dedicated to space or airborne operations.

Keywords: acousto-optical nonlinearity, two-phonon light scattering, crystalline calomel cell, optical spectrum analysis, spectral resolution.

1 INTRODUCTION

The history of acousto-optical dispersive components originates from the optical filters based on acousto-optical cells (AOCs), which were first developed in the late 60s past century. Since then, both collinear and non-collinear geometries of the AOCs for those filters have been evolved continuously. Owing to physical properties of modern crystals, the collinear AOCs are more restricted in the number of potentially acceptable crystals related to the specific crystallographic point groups [1]. However, practically almost only crystals, belonging to the point group 3m, are available for collinear interaction. Together with this, the non-collinear AOCs can be based on much larger number of crystals than the collinear ones. Then, there is a peculiarity in usage of the above-noted geometries inherent in the AOCs. One can say that collinear AOCs exhibit usually remarkably higher spectral resolution combined with relatively restricted efficiency [2], while the non-collinear AOCs often demonstrate high relative efficiency associated unfortunately with moderate spectral resolution. In a view of this, an opportunity for combining the advantages peculiar to each of the enumerated geometries looks rather desirable.

In recent years, one of the most frequently used materials for non-collinear AOCs is the tellurium dioxide (TeO_2) crystal. In comparison with such widely used crystalline materials like, for example, lithium niobate, lead molybdate, gallium phosphide etc., the important advantage of a TeO_2 crystal consists in extremely low acoustic velocity $V \approx 0.616\times10^5$ cm/s for the slow shear elastic mode passing along the $[1\bar{1}0]$-axis, which provides very high figure of acousto-optical merit $M_2 \approx 1200\times10^{-18}$ s^3/g [3]. Even with the demerit of very high /~290 dB/(cm·GHz^2) / acoustic attenuation, the tellurium dioxide allows us to reach ~ 100% efficiency of one-phonon light scattering at not too high acoustic power density. Moreover, this crystal admits a two-phonon light scattering as well. However, this crystal has rather important acousto-optical disadvantage as well. The above-mentioned parameters are indissolubly connected with light beams propagation in the vicinity of its optical axis, where the TeO_2-crystal exhibits significant optical activity, so that those beams have to be very accurately polarized, circularly or elliptically, as the case requires.

The other crystalline material potentially suitable for designing modern AOCs is the calomel (Hg_2Cl_2) single crystal. Its parameters, namely: the acoustic velocity $V \approx 0.347 \times 10^5$ cm/s for the slow shear mode passing along the [110]-axis; the figure of acousto-optical merit $M_2 \approx 1.5 – 2.0 \times 10^{-15}$ s^3/g; and the acoustic losses ~ 230 dB/(cm GHz^2) exceed significantly performances of the above-mentioned ordinary materials and tellurium dioxide. Potentials of the calomel are not connected with any problems of optical activity and look even more attractive than the parameters of tellurium dioxide. This is why we have selected the calomel crystal for our pioneer studies in nonlinear acousto-optics. However, the calomel crystal has elevated refractive indices, and it is chemically toxic in handling. Nevertheless, both these problems can be resolved with the help of the corresponding optical coating.

Physical properties of this material had been widely investigated from the middle of the 70s [4,5]. During the last decade, the calomel had been studied in connection with the creation of AOCs and acousto-optical filters (AOFs). The characterization of calomel-based AOCs operating over a longitudinal acoustic mode has been carried out, and the efficiencies of about 20% at 0.9 W radio-frequency power [6,7] have been achieved. Then, the calomel-based AOF with the collinear configuration has also been used in the mid-infrared range for pulse shaping [8]. This type of AOFs with the collinear AOCs has also been exploited for imaging purposes in biomedical applications utilizing the slow shear acoustic mode passing along the [110]-axis [9].

Past year, principally new features of a square-law parametric nonlinearity inherent in the non-collinear two-phonon light scattering had been revealed [10]. These features can be observed under action of the acoustic waves of finite amplitude in crystals with optical birefringence. The detected peculiarities of this parametric nonlinearity manifest themselves at quite limited acoustic power in crystalline materials in the presence of linear acoustic attenuation. The recently identified additional physical degree of freedom [10], unique to the non-collinear two-phonon light scattering, can be exploited for designing a specific calomel-based AOC. Moreover, such an AOC can double the spectral resolution of the acousto-optical spectrum analysis due to the application of two-phonon processes.

The improvement of the spectral resolution in tunable acousto-optical filters can be applied to almost every spectroscopic application. For example, a higher spectral resolution can improve the results used in hyperspectral imaging, where the acousto-optical devices are already in use as monocromators and optical band-pass filters [11].

Also, the possibility of analyzing the blue edge of the visible range and the enhancement of the spectral resolution will enable the acousto-optical spectrographs to help in many astrophysical fields. For example, it can allow us to perform asteroseismological studies of diverse kinds of variable stars (γ Doradus, δ Scuti, roAp, β Cephei) [12,13] by resolving their periodic spectral change; or to analyze the stellar activity by measuring the intensity of the chromospheric Ca H and K emission lines [14].

The goal of our investigations presented here consists in studying the most essential properties inherent in the nonlinear phenomenon under consideration. We try to clarify the role of changes in central acoustic frequencies and plausible acoustic attenuation per aperture of the calomel-made AOC using that additional degree of freedom. Then, practically important problem exists with relatively narrow frequency and spectral bandwidths of the AOC exploiting the non-collinear two-phonon light scattering. Based on high acousto-optical efficiency of calomel, the bandwidth of the calomel-made AOC can be potentially extended at the expense of decreasing the efficiency of that AOC in part. Here, we try to demonstrate the possibility of reaching these goals during a new set of

proof-of-principle experiments with a wide-aperture calomel-based AOC. The obtained experimental data can be considered as the confirmation of the developed approaches.

In section 2, an advanced theory for the non-collinear two-phonon light scattering, which includes the contribution of linear attenuation for the acoustic wave of finite amplitude, is presented. Section 3 is devoted to local analysis for the first maxima of two-phonon light scattering and to characterization of the appearing nonlinear apodization. Section 4 includes our approach to the resolving power inherent in a dispersive component represented by the calomel-made AOC exploiting the non-collinear two-phonon light scattering. Section 5 represents various theoretical estimations for a dispersive component based on the calomel-made crystalline AOC. The experimental set-up and proof-of-principal experimental data are described in Section 6; where, in particular, the obtained results are compared with the best known modern data. Briefly explained conclusive remarks are placed in Section 7.

2 TWO-PHONON LIGHT SCATTERING BY THE ATTENUATING ACOUSTIC WAVES OF FINITE AMPLITUDE

Recently, a quasi-stationary two-phonon Bragg light scattering by acoustic waves of finite amplitude had been investigated (for the first time) [10]. In particular, significantly nonlinear evolution of the light wave amplitude $C_2(x)$, deflected into the second order, had been described (here, x is the spatial coordinate along the direction of light propagation). Now, we improve that analysis taking into account the effect of acoustic losses in a medium. In so doing, we consider the linear attenuation of an acoustic wave passing along the z-axis (i.e. along the aperture of an AOC), which can be described by a one-dimensional wave equation for the acoustic wave complex amplitude U

$$\frac{\partial U}{\partial z}+\frac{1}{V}\frac{\partial U}{\partial t}=-\alpha U\,. \tag{1}$$

here, V is the acoustic wave velocity and the amplitude factor α describes the linear acoustic attenuation; then, $U(z = 0, t) = U_0$ is the boundary condition for the acoustic wave amplitude. With $\alpha \neq 0$, Eq.(1) has simple solution $U(z) = U_0 \exp(-\alpha z)$ in the tracking coordinates, and Eq.(6) from Ref. [10] can be re-written in the form, which includes now acoustic losses,

$$C_2(x,\alpha)=\frac{\sigma^2\exp[(b_1+i\eta)x]}{(b_1-b_2)(b_1-b_3)}-\frac{\sigma^2\exp[(b_2+i\eta)x]}{(b_1-b_2)(b_2-b_3)}+\frac{\sigma^2\exp[(b_3+i\eta)x]}{b_1b_2-b_1b_3-b_2b_3+b_3^2}\,. \tag{2}$$

The factors b_k (k = 1,2,3) are the complex-valued roots of the algebraic characteristic equation

$$b^3+i\eta\,b^2+2\sigma^2\,b+i\eta\,\sigma^2=0\,, \tag{3}$$

which includes dependences on the coordinate z; here, σ is the acoustic power parameter and η is the angular-frequency mismatch. Equation (2) gives the general solution that satisfies the following boundary conditions

$$C_2(x=0)=0\,,\qquad (dC_2/dx)(x=0)=0\,,\qquad (d^2C_2/dx^2)(x=0)=\sigma^2\,. \tag{4}$$

Then, $\sigma(z)=qU(z)=\pi(\lambda\cos\theta)^{-1}\sqrt{M_2P(z)/2}$, q is the constant of acousto-optical interaction (AOI), θ is the angle of incidence for an external plane monochromatic light wave, λ is the incident light wavelength, P is the acoustic field power density, M_2 is the figure of acousto-optical merit for an acousto-optical material.

The expression for the complex amplitude $C_2(x, \alpha)$ can be simulated numerically in terms of two dimensionless coordinates σx and ηx, characterizing the acoustic power density and the frequency mismatch at the exact angular alignment; the linear acoustic losses can be also described by a one dimensionless parameter a = αz. Numerically created 3D-distributions in Fig. 1 demonstrate the effect of linear acoustic attenuation for z = 1 cm and α = 0**,** 0.3, and 0.5 cm^{-1}. These distributions depict theoretical possibility of reaching a set of the unit-level maxima, i.e. ~100% efficiency of light scattering into the second order, in some isolated points along the σx-axis. Comparison of these plots with one another shows that the effect of acoustic losses in a medium leads only to scaling the nonlinear distributions along the coordinate σx. The last statement follows from the simplified real-valued solution

$$C_2\,(x,\alpha,\eta=0)=\sin^2\left[(U_0\,x/\sqrt{2})\cdot\exp\,(-\alpha\,z)\right], \tag{5}$$

describing a regular sequence of the unit-level maxima whose periodicity depends on the parameter a = α z. Together with this, the mismatch profiles related to first three unit-level maxima of a two-phonon light scattering are non-perturbed by linear acoustic losses, i.e. they are the same at any magnitude of α.

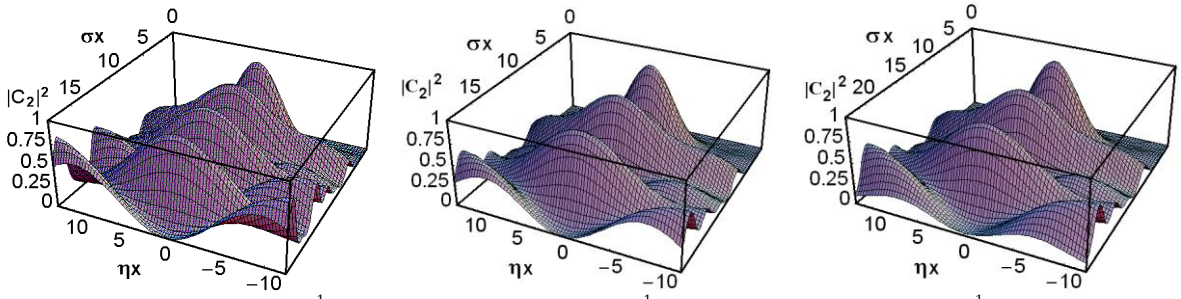

Fig. 1. The 3D- bandshapes for the non-collinear two-phonon AOI in three cases of linear acoustic attenuation: (a) is for α = 0 cm^{-1}, (b) is for α = 0.3 cm^{-1}, and (c) is for α = 0.5 cm^{-1}; evolution along the axis σx reflects nonlinearity of this phenomenon.

At the same time, numerical calculations show the locations of the unit-level maxima of a two-phonon light scattering with various acoustic attenuation α ≥ 0 along the axis σx, see Fig.2. At the points $(\sigma x)_1$ of light intensity distributions, belonging to the 1-st unit-level maxima at any magnitude of α ≥ 0, all the mismatch profiles are the same in dimensionless units, see Fig.3. All these profiles have the same widths $\eta x_{\pm}$ = ±3.5703 at the 0.405-level. Using the previously developed consideration [10], one can find two-side frequency bandwidth

$$\Delta f \approx 7.14\, n_0 V^2/(4\pi\lambda\, f_0\, L) \approx 0.5685\, n_0 V^2/(\lambda\, f_0\, L)\,. \tag{6}$$

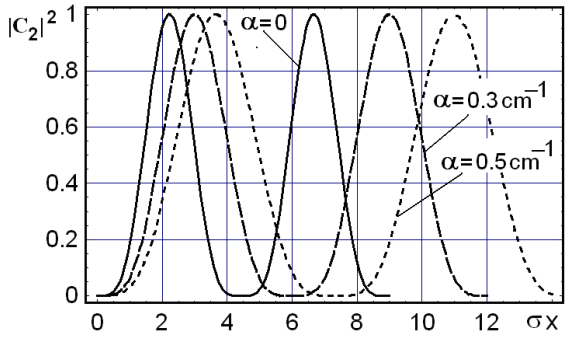

Fig. 2. The scattered light intensity vs. dimensionless coordinate σx with z = 1 cm and α = 0, 0.3, 0.5 cm^{-1}; the 1-st maxima are placed at $(\sigma x)_1 \approx$ 2.22, 2.9986 and 3.6625.

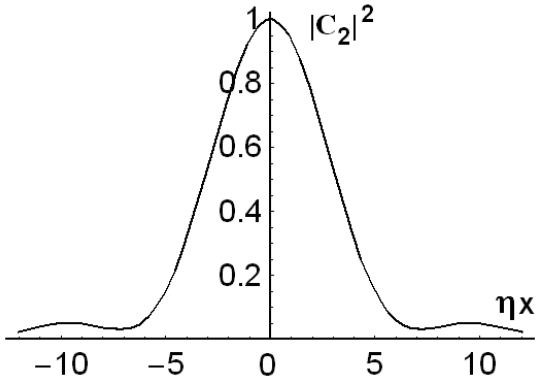

Fig. 3. All the profiles are the same in dimensionless units; one yields the same widths $\eta x_{\pm}$ = ±3.5703 at the 0.405-level.

3 LOCAL ANALYSIS AND THE FIRST MAXIMA OF TWO-PHONON LIGHT SCATTERING

Within linear acousto-optics, one can use standard approach to estimating the action of linear acoustic attenuation using the Fourier transformation of exponentially falling down distribution at the AOC's output facet. The Fourier transformed signal gives a resolvable spot profile in the focal plane of the integrating lens within classical scheme of spectrum analyzer [15]. In so doing, the light intensity profile of a spot gives the main lobe width and level of side lobes characterizing both the resolution and the dynamic range of an optical system. In our case, one should estimate the combined effect provided by acousto-optical nonlinearity and linear acoustic losses in AOC. For this purpose, we compare with one another light distributions $C_2(x, \alpha)$ along coordinate σx in the vicinity of various points $(\sigma x)_1$ peculiar to the first unit-level maxima for a few magnitudes of α. The preliminary analysis has shown that similar light distributions are significantly non-uniform along AOC's aperture, so that the final Fourier transformed signals are not optimal in the focal plane of a lens. This is why those values $(\sigma x)_1$ had been somewhat exceeded with the purpose of making an optimization. The goal of such an optimization consists in achieving as much as possible more symmetrical light distributions at the output facet of an AOC. However, local maximum for each of these output light distributions is slightly shifted from a point corresponding to the middle between two falling down wings of the corresponding distribution.

To make more concrete our consideration an appropriate acousto-optical crystalline material has to be selected for the further analysis. During the selection of a material, a few possibilities of exploiting either longitudinal or shear elastic modes, passing along various crystallographic directions, had been estimated. The analysis has shown that one of the best options for performing experiments, motivated by very high efficiency of scattering and not too high acoustic frequency for excitation, is the calomel (α-Hg_2Cl_2) single crystal. This crystal belongs to the 4/mmm – tetragonal symmetry group. It has spectral transmission band $\Delta\lambda$ = 0.38 – 28 μm and a pair of dispersive refractive indices, whose main values are N_O = 1.9634 and N_E = 2.6217 at the wavelength λ = 633 nm; its material density is equal to $\rho \approx 7.2$ g / cm^3 [5]. This crystal is potentially suitable for effective non-collinear two-phonon light scattering and allows pure slow-shear elastic mode with the wave vector $\vec{K} \| [110]$, the displacement vector $\vec{u} \| [1\bar{1}0]$, the phase velocity $V_S \approx 0.347\ 10^5$ cm/s, and the acoustic wave attenuation factor $\Gamma \approx 230$ dB / (cm GHz^2), which gives the amplitude factor α in the form of α (cm^{-1}) = 0.1152 Γ f^2.

At this point we will not motivate in detail our selection of the level B for total linear acoustic losses per optical aperture D of the calomel-made AOC. Nevertheless, together with traditionally exploited value B = 4 dB [16], the values B = 6 and 8 dB will be taken as well in a view of principle possibility to correct them later by the needed apodization. Choosing B = 4, 6 or 8 dB allows us to avoid unnecessarily strong limitations for this stage of studies. More detailed analysis can be started proceeding from the optical aperture D = 5.2 cm of the AOC, restricted by an available sample of the chosen crystalline material. Taking the above-mentioned levels of losses B per optical aperture, one can find the central frequencies for a two-phonon light scattering as $f_0 = \sqrt{B/(\Gamma D)}$, so that one yields $f_0 \approx$ 57.8, 71.0, and 82.6 MHz as well as $\alpha \approx$ 0.08851, 0.1336, and 0.1808 cm^{-1}, respectively. For this triplet of the central acoustic frequencies, the first unit level maxima at the points $(\sigma x)_1$ = 2.427, 2.539, and 2.662 represent trial values for the following optimization.

After performing the above-proposed optimization, one can take $(\sigma x)_{1,Opt}$ = 2.785, 2.965, and 3.200, which provide more symmetric distributions presented in Fig. 4. With D = 5.2 cm, the desirable new maxima are located at the points $z_{max} \approx$ 2.308, 2.162, and 2.019 cm, respectively. An example of the corresponding 3D-distribution with the f_0 = 71.0 MHz is presented in Fig. 5.

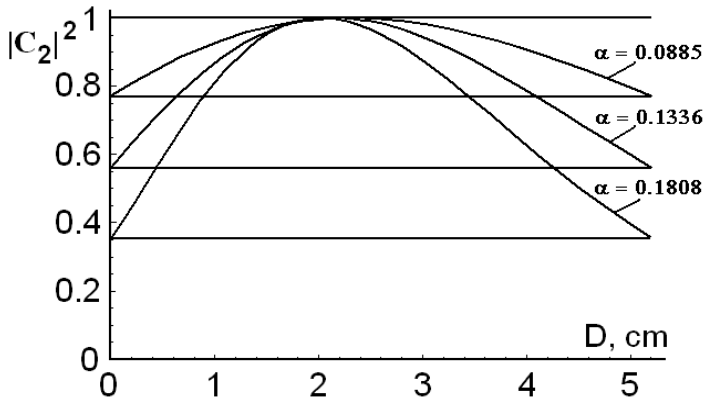

Fig. 4. Optimized 2D-profiles of the light distributions at the output facet of the calomel-made AOC at $f_0 \approx 57.8$, 71.0, and 82.6 MHz with $\alpha \approx 0.8851$, 0.1336, and 0.1808 cm^{-1}.

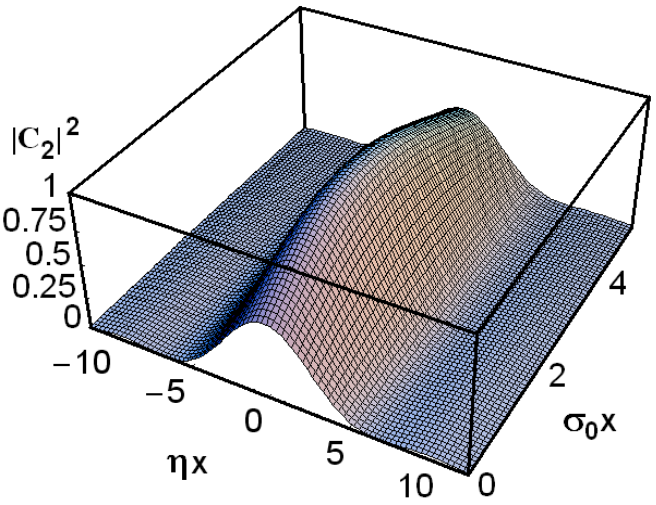

Fig. 5. An example of an optimized 3D-profile of the issuing light distribution with $f_0 = 71.0$ MHz and $\alpha \approx 0.1336$ cm^{-1}**.**

Looking at these plots, one can find that the combined influence provided by acousto-optical nonlinearity and linear acoustic losses leads to the some equivalent apodization of initially flat incident light beam, see solid lines in Fig. 4.

To describe the Gaussian apodization for a flat incoming light beam with the field amplitude A_0 we take the origin of the physical coordinate z across that beam so that the point z = 0 is associated with the plane of piezoelectric transducer in an AOC. Then, one can introduce y = z / D as the normalized dimensionless coordinate along the physical aperture D (measured in centimeters) of an AOC. Thus, $y \in \{0,1\}$ and one can write

$$A = A_0 \exp[-\chi (z - 0.5D)^2] = A_0 \exp[-\beta (y - 0.5)^2], \quad I(y) = |A_0|^2 \exp[-2\beta (y - 0.5)^2]. \quad (7)$$

Here, χ and $\beta = \chi D^2$ are physical and dimensionless profile parameters for the apodizing Gaussian function; possible variations of I(y) are governed by the profile parameter β. In particular, for the plots presented in Fig. 4, one can suggest the centered approximations with $\beta = 0.50$, 1.15, and 2.10, see Fig. 6, to avoid unnecessary strong consideration at this stage of studies. The shape of light field distribution A(u) peculiar to an individual resolvable spot in the Fourier-transform plane, i.e. in a focal plane of the integrating lens, can be estimated analytically as

$$\text{a)}\ A(u)=\int_0^1 \exp\,[-\beta(y-0.5)^2]\,\exp(-2i\pi u\,y)\,dy, \qquad \text{b)}\ A(u=0)=\sqrt{\frac{\pi}{\beta}}\ Erf\ (0.5\sqrt{\beta}). \quad (8)$$

The spatial dimensionless coordinate u is centered on a maximum of that distribution, and u = w D / λ F, where w is the physical spatial coordinate in the focal plane and F is the focal distance of the integrating lens. Using Eqs.(8), the normalized distribution I(u) of light intensity peculiar to an individual resolvable spot in the focal plane of the integrating lens can be written as I(u) = A(u) A^{*}(u) A^{-2}(u = 0) i.e.

$$I(u)=-\frac{1}{4}\ Erf^{-2}\left(\frac{\sqrt{\beta}}{2}\right)\exp\left[-\frac{2\pi^2u^2}{\beta}\right]\left\{Erfi\left[\frac{2\pi u-i\beta}{2\sqrt{\beta}}\right]-Erfi\left[\frac{2\pi u+i\beta}{2\sqrt{\beta}}\right]\right\}^2. \quad (9)$$

In the case of β ≈ 0, an ideal normalized profile of a resolvable spot has full width equal to unity in terms of the dimensionless coordinate u at the intensity level 0.405. The required corrections to theoretical width of a resolvable spot, conditioned by the presence of linear acoustic losses when β ≠ 0, can be made using the correction factor κ of apodization. The needed values of this factor are: κ ≈ 1.019, 1.043, and 1.080**,** i.e. the main lobe has broadening by about 1.9, 4.3, and 8.0% due to the effect of linear acoustic losses for β = 0.50, 1.15, and 2.10, respectively. Thus, the performed apodizations, provided by properties of an AOC near the first maximum, are not deep enough (they equal to -14 ÷ -17 dB for the first side lobe) to improve significantly the dynamic range of potential optical spectrum analysis, see Fig. 7.

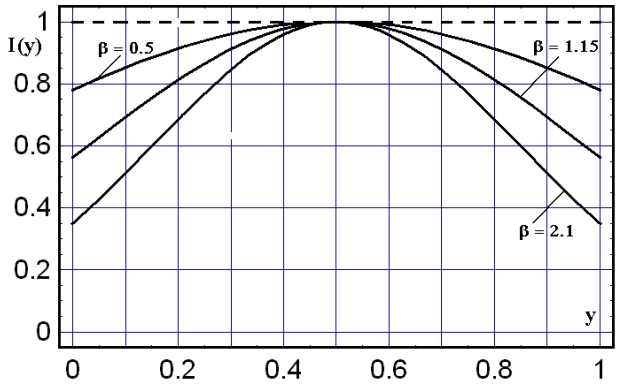

Fig. 6. Theoretical profiles for the Gaussian centered approximations with the dimensionless apodization parameters β = 0.50, 1.15, 2.10.

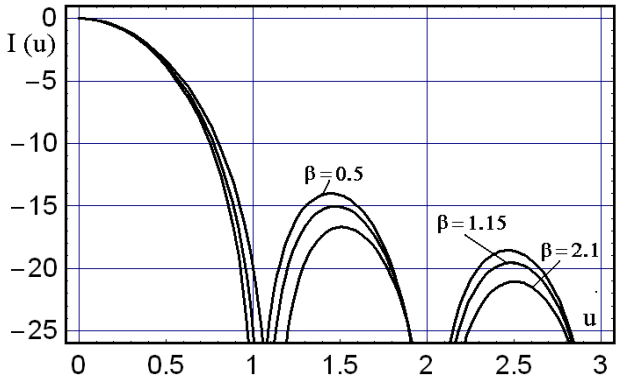

Fig. 7. Theoretical logarithmic profiles of resolvable spots with the dimensionless apodization parameters β = 0.50, 1.15, 2.10.

4 RESOLVING POWER INHERENT IN A DISPERSIVE COMPONENT REPRESENTED BY THE AOC

In physical optics, the resolving power (RP) is expressed usually as the ratio $R = \lambda / \delta\lambda$ [17], where λ is the incident light wavelength and $\delta\lambda$ is the spectral resolution. It is one of the most important parameters peculiar to various dispersive optical components, including both traditional static diffraction gratings and AOCs, representing dynamic diffraction gratings. Besides that, the RP of a static diffraction grating can be characterized by the product $R = |\nu| N$, where ν is the order of diffraction and N is a number of the lighted slits. In fact, N includes the lighted aperture d[mm] of that grating and the slit density S[lines/mm] because of $N = S d$. Combining these simple formulas, one arrives at

$$\delta\lambda = \lambda/(|\nu| S d) = \lambda/(|\nu| N). \tag{10}$$

In acousto-optics, the RP of an AOC as the dynamic diffraction grating depends significantly on the chosen regime of light scattering. The key value here is a number of the lighted slits, which has various determinations caused by a regime. The non-collinear two-phonon light scattering occurs at the acoustic wave frequency f_0 [18], specific to the needed central optical wavelength λ_0, so that one can write

$$f_0 = V b / \lambda_0 , \tag{11}$$

where $b = \sqrt{|n_0^2 - n_1^2|}$ is the birefringence factor, $n_0(\lambda) \neq n_1(\lambda)$ are the current refractive indices of a crystal. Thus, the number of slits N can be expressed as $N = D f_0 / V$, where the ratio f_0 / V describes the inverted acoustic wavelength, which is an analogue of the slit density. Substituting this formula into Eq.(10), one yields

$$\delta\lambda = V \lambda_0 /(|\nu| D f_0). \tag{12}$$

Then, using Eq.(11), one will have $\delta\lambda = \lambda_0^2 / (|\nu| b D)$. Therefore, in an acoustically low-loss case with $|\nu| = 2$ peculiar to the non-collinear two-phonon light scattering, the spectral resolution takes the form

$$\delta\lambda = \lambda_0^2/(2 b D). \tag{13}$$

There are a few factors limiting the RP of an AOC, which can be represented as functions of the central optical wavelength λ_0 inherent in the chosen regime of light scattering. The first of them is directly follows from Eq.(13) in the form

$$R_1 \leq 2 b D / \lambda_0 , \tag{14}$$

where the optical aperture D serves as a parameter.

Then, the acoustic beam divergence, as it is passing through the light beam, is under the second geometrical limitation for the RP. Physically, it is the requirement upon the piezoelectric transducer to operate in the acoustic Fresnel zone restricting the acoustic beam divergence. This limitation couples the piezoelectric transducer length L (that represents the length of acousto-optical interaction in fact) with the distance from that transducer to the point of half power level in the

near-field zone of the acoustic waves. Practically, this distance is equivalent to the optical aperture D, so that one can write $D = L^2 f_0 / (2V)$. Substituting the last expression for D together with Eq.(11), into Eq.(14), one yields

$$R_2 \le \frac{2 b L^2 f_0}{\lambda_0 2V} = \frac{b^2 L^2}{\lambda_0^2} \ . \tag{15}$$

The third limitation is connected with the linear acoustic attenuation. It can also be represented as a function of the central optical wavelength. If the level of acoustic attenuation B[dB] per the optical aperture D of a cell is acceptable, the size of allowable optical aperture is equal to $D \le B\, \Gamma^{-1} f_0^{-2}$. Substituting this formula into Eq.(14) and using Eq.(11), one arrives at the following expression

$$R_3 \le \frac{2 B\,[dB]\, \lambda_0\,[\mu m] \times 10^{14}}{b\, \Gamma\,[dB/(cm \cdot GHz^2)]\, (V\,[cm/s])^2} \ . \tag{16}$$

Thus a triplet of the above-mentioned independent limitations restricts the RP of an AOC. In the particular case of a two-phonon light scattering, one can take a set of rather effective and available materials. However, one can see from Eqs.(14) – (16) that these limitations for the RP always include the ratio b/λ_0, i.e. their spectral dependencies are determined by a behavior of the dispersive birefringence factor b inherent in a material. Because of Eq.(11) gives the expression $b/\lambda_0 = f_0/V$, the obtained limitations can be expressed in the same terms as

$$\text{a) } R_1 \le \frac{2 f_0 D}{V} \ , \quad \text{b) } R_2 \le \frac{f_0^2 L^2}{V^2} \ , \quad \text{c) } R_3 \le \frac{2 B\,[dB] \times 10^7}{\Gamma\,[dB/(cm \cdot GHz^2)]\ f_0\,[MHz]\, V\,[cm/s]} \ . \tag{17}$$

Equations (17) demonstrate that the RP of an AOC depends significantly on the chosen acoustic frequency. An acceptable size of the aperture D depends on various physical factors, the most important of which is the acoustic attenuation.

Now, we are coming to principally new step in studying the nonlinearity of non-collinear two-phonon AOI [10], see Fig. 8. This step can be represented for the corresponding processes of scattering in terms of two surfaces for the refractive indices of ordinary (see the internal dark sphere) and extraordinary (see the external faint ellipsoid) light waves for a tetragonal crystal at the fixed optical wavelength λ_0 (here, the calomel crystal is taken as an example with $N_E \ge N_O$). The sizes of both sphere and ellipsoid will be varied depending on λ_0 due to remarkable dispersion of the crystalline material within potential optical range. The vertical axis in Fig. 8 is oriented along the optical axis [001] of that crystal, while orientation for a pair of the horizontal axes depends on the chosen elastic modes. For the calomel crystal, in particular, they can be taken as [110] and $[1\bar{1}0]$ axes for the slow shear mode. Then, this figure represents the vector diagram, illustrating an opportunity for the two-phonon light scattering through various angles; which includes an optimal acoustic frequency with the birefringence factor b adequate to the chosen λ_0. A triplet of vectors, going from the geometric center of surfaces, represents the optical wave vectors describing the corresponding orders of light scattering, whereas a pair of the sequential acoustic wave vectors $\vec{K}$ reflects the two-phonon process. The tilt angle ψ characterizes an angle between the optical axis and the geometrical plane including all the optical and acoustic wave vectors. The availability of the angle ψ reflects the existence of an additional physical degree of freedom inherent in the nonlinearity of the two-phonon light scattering.

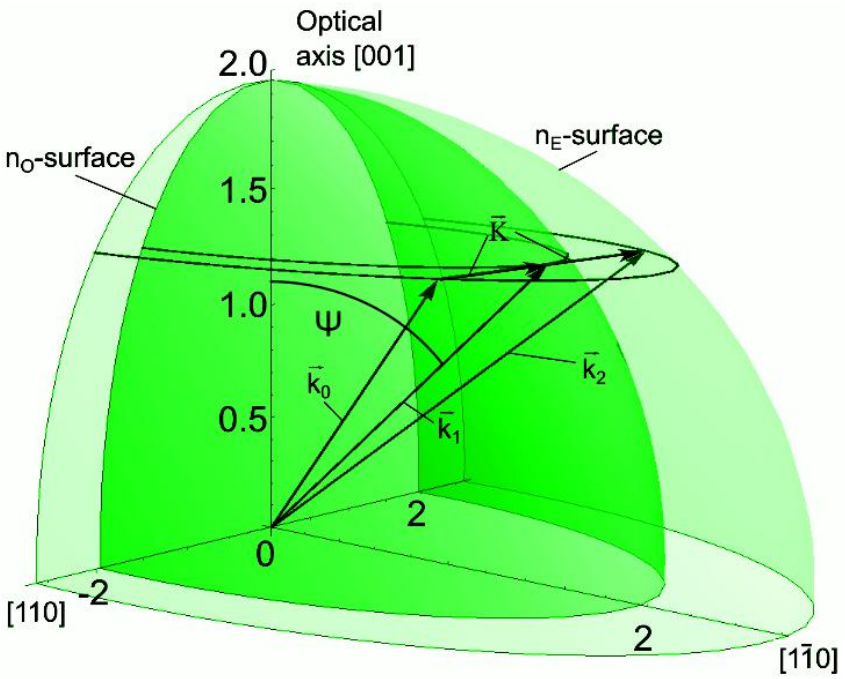

Fig. 8. The vector diagram for two-phonon light scattering in calomel where ψ is the tilt angle.

This degree of freedom permits the fixed frequency f_0 to exert control over various optical wavelengths scattered through different angles. In this case, one has to consider two pairs of surfaces peculiar to the refractive indices of ordinary and extraordinary light waves for a tetragonal crystal and each similar pair of surfaces will correspond to an individual light wavelength.

Calomel is a uniaxial crystal, so that $n_O \equiv N_O$ is the main refractive index for the ordinary state of polarization whose 3D-distribution is a sphere. The refractive index n_E for the extraordinary polarization ($n_E < n_O$) depends on a direction of light propagation in a crystal, and its 3D-distribution has the form of an ellipsoid. We are interested in rather small tilts from the [001]-axis, therefore, one can consider the angle $\psi \in [\, 0, \pi / 2]$ of a tilt from the [001] -axis. Considering the geometry yields and using Eq.(11), one can obtain

$$\tan\psi = \frac{\lambda_0 \; f_0 \; N_E}{N_O \sqrt{V^2 (N_E^2 - N_O^2) - \lambda_0^2 \; f_0^2}} . \qquad (18)$$

Now, keeping in mind requirements of the best achievable spectral resolution and resolving power, the detailed analysis can be performed proceeding from the optical aperture D of the AOC, restricted by an available sample of the chosen crystalline material with the given factor Γ of acoustic attenuation. Taking the above-motivated value B dB/aperture, one can find the central frequency for a two-phonon light scattering as $f_0 = \sqrt{B/(\Gamma D)}$. Then, the chosen calomel crystal gives the fixed acoustic velocity V = 0.347 × 10^5 cm/s and the main refractive indices $N_E(\lambda)$ and $N_O(\lambda)$. The dispersion of main indices in calomel is given by [19]

$$\text{a)}\; N_O = \sqrt{1 + \frac{2.595 \cdot \lambda^2}{\lambda^2 - 0.03648}} , \qquad \text{b)}\; N_E = \sqrt{1 + \frac{2.490 \cdot \lambda^2}{\lambda^2 - 0.08237} + \frac{2.479 \cdot \lambda^2}{\lambda^2 - 0.03803}} , \qquad (19)$$

where λ must be expressed in micrometers. These indices should be substituted in Eq.(18) to explain the current (local) refractive indices n_O and n_E as well as the tilt angle ψ mentioned above at the chosen central frequency f_0. After that, one has to note that now $b(\lambda) = \sqrt{n_E^2(\lambda) - n_O^2(\lambda)}$, as well as this factor includes the dependence on the frequency f_0. Using these details, one can come back to estimating the RP as function of aforementioned limitations.

The length L and central frequency f_0 of Bragg acousto-optical interaction in a crystal are restricted by the following well-known inequality for Klein-Cook parameter $Q = 2\pi\lambda L f_0^2 / (n_0 V^2) >> 1$ [20]. In calomel, for the slow shear mode passing along the [110]-axis with $V = 0.347\times10^5$ cm/s, and $n_0 = 2.0826$ at λ = 405 nm, one can find $f_0 = \sqrt{B/(D\Gamma)} \approx 50$ MHz and $L_{min} >> 0.0038$ Q cm. Taking the limiting value Q = 4 π, as it had been recommended in Ref. [20], one yields $L_{min} \geq 0.05$ cm and can take, for example, $L_{min} \approx 0.2$ cm with a safety margin. Consequently, with L ≈ 0.2 cm the central acoustic frequencies $f_0 \geq 50$ MHz can be chosen without any doubts in Bragg character of light scattering.

With choosing B = 4, 6, and 8 dB, one can calculate $f_0 \approx 57.8$, 71.0, and 82.6 MHz, respectively, from the above-noted formulas for the aperture D = 5.2 cm. Then, using Eq.(18) together with Eq.(19), one can find the magnitudes for tan ψ = T (λ_0, f_0) in calomel; namely, T(405 nm, 57.8 MHz) ≈ 0.0445, T(405, 71.0) ≈ 0.0546, T(405 nm, 82.6 MHz) ≈ 0.0636, T(633 nm, 57.8 MHz) ≈ 0.0812, T(633, 71.0) ≈ 0.0995 , and T(633 nm, 82.6 MHz) ≈ 0.1162. With these data, one can numerically estimate the limitations restricting the RP for the calomel-based AOC. Applying Eqs.(17), one can obtain the frequency dependences presented in Fig. 9.

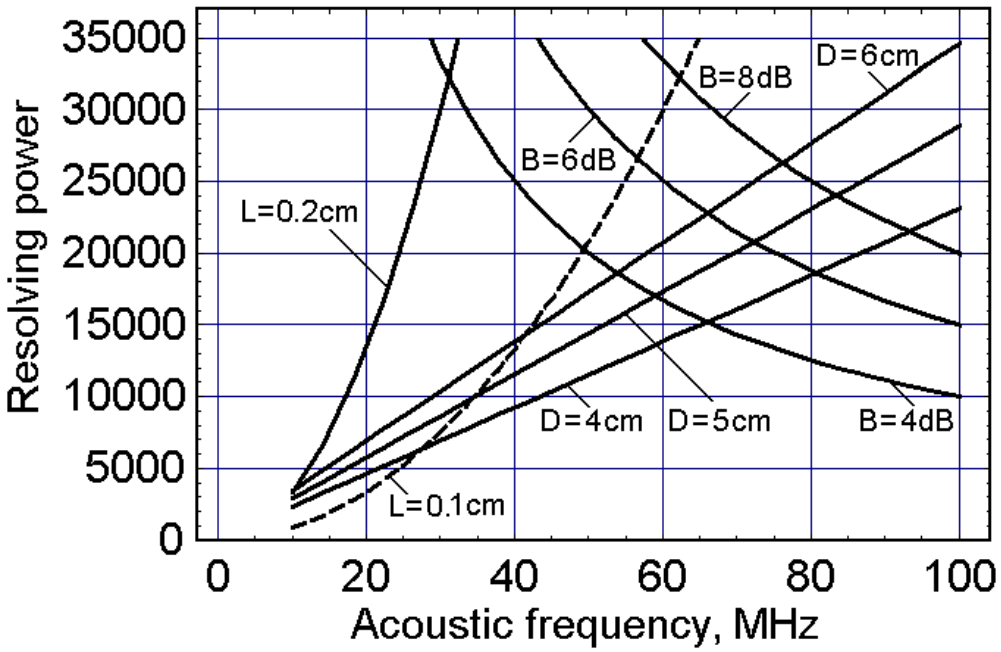

Fig. 9. Resolving power of the calomel-based AOC vs. the optical aperture D, the length of acousto-optical interaction L, and the acoustic attenuation parameter B.

It is seen from the plots in Fig. 9 that one can expect for the RP the following theoretical estimations: R(B = 4 dB, 57.8 MHz) ≈ 17000, R(B = 6 dB, 71 MHz) ≈ 20000, and R(B = 8 dB, 82.6 MHz) ≈ 25000. Hence, at λ_0 = 405 nm one yields $\delta\lambda_0 \approx 0.238$ Å with B = 4dB, $\delta\lambda_0 \approx 0.2025$ Å with B = 6 dB, and $\delta\lambda_0 \approx 0.162$ Å with B = 8 dB, respectively.

5 THEORETICAL ESTIMATIONS OF A DISPERSIVE COMPONENT BASED ON THE CALOMEL-MADE CRYSTALLINE AOC

Now, one can estimate potential performances of a dispersive component, based on the calomel-made AOC with the optical aperture D = 5.2 cm**.** The goals are designing similar crystalline AOC and carrying out the needed proof-of-principle experiments with this AOC.

5.1. Effect of the acoustic beam divergence

The angular divergence of the acoustic beam can be considered via estimating the length X of Fresnel acoustic zone when the unknown radiating acoustic aperture is equal to R. These values are connected with one another as $X = R^2 f_0 / (2 V)$ [21]. If it is granted that the acoustic beam belongs to Fresnel acoustic zone and X = 5.2 cm at the lower of the above-chosen acoustic frequency $f_0 \approx 57.8$ MHz, one can find for α-Hg_2Cl_2 that $R \approx \sqrt{2 V_S X / f_o} \approx 0.08\, cm$. Thus with $R \geq 0.10$ cm, which is rather typical value in practice, one can conclude that the expected angular divergence of acoustic beam is definitely small to be neglected. Consequently, the plane-wave approximation can be used for characterizing the acoustic beam propagation. The exact angular divergence of acoustic beam in the calomel non-collinear AOC at $f_0 \approx 57.8$ MHz can be estimated as well. A reliable spatial size of the initial acoustic beam aperture that we will consider is close to L ≈ 0.2 cm. With $V = 0.347 \times 10^5$ cm/s, one can calculate the corresponding acoustic wavelength $\Lambda = V / f_0 = 0.60 \times 10^{-3}$ cm and the angle of acoustic beam divergence $\varphi = \Lambda / L = 0.30 \times 10^{-2}$ rad ≈ 0.172º to conclude that the angular divergence of the acoustic beam can be omitted.

5.2. General estimations for the calomel-made AOC

For the calomel-made AOC with D = 5.2 cm and $L_{min} \approx 0.2$ cm, the theoretical estimations have been performed and summarized in Table 1. These estimations are related only to the first of recently found maxima [10] in a distribution of light scattered into the second order due to non-collinear two-phonon AOI, see Fig. 8. One can see from this table that rather high spectral resolution can be achieved in calomel with the exploitation of the pure slow shear elastic mode S[110]. Consequently, these data show that further development of a new approach to optical spectrum analysis is definitely desirable due to its improved spectral resolution. In acousto-optics, the spectral and frequency bandwidths as well as the frequency and spectral resolutions are connected with one another by the following relations $\Delta\lambda = \Delta f\, \lambda / f_0$ and $\delta\lambda = \delta f\, \lambda / f_0$, respectively. In particular, using Eqs.(6) and (12), one can find the spectral bandwidth $\Delta\lambda$, determine the frequency resolution as $\delta f = V/(2 D)$, and then obtain the number of resolvable spots $N = \Delta f / \delta f = \Delta\lambda / \delta\lambda$.

Table 1. Theoretical estimations with: $\delta f_{Th} \approx 3.337$ kHz; $V = 0.347\ 10^5$ cm/s; type of the elastic mode is S [110]; the product $2\, b\, D = \lambda^2 / \delta\lambda$ includes the birefringence factor b.

λ, nm	**n_O**	**f_0, MHz**	**Δf_{Th}, MHz**	**B, dB**	**N_{Th}, spots**	**$\Delta\lambda_{Th}$, Å**	**$\delta\lambda_{Th}$, Å**	**2 b D, cm**
405	2.0826	57.8	3.05	4.0	913	213.4	0.23375	0.7017
		71.0	2.48	6.0	743	141.4	0.19035	0.8617
		82.6	2.13	8.0	639	104.5	0.16357	1.0028
633	1.9634	57.8	1.84	4.0	571	201.2	0.36533	1.0961
		71.0	1.49	6.0	448	133.3	0.29751	1.3468
		82.6	1.27	8.0	385	98.5	0.25557	1.5668

5.3. Figure of acousto-optical merit for the non-collinear two-phonon light scattering in calomel crystal

Generally, estimating the figure of acousto-optical merit M_2 for the above-chosen geometry in α-Hg_2Cl_2 single crystal and the slow shear acoustic mode with the normalized displacement vector $\vec{u} = (1, -1, 0)/\sqrt{2}$, the acoustic wave vector $\vec{K} \| [110]$, and the deformation tensor γ had been recently performed [10]. Therefore, it is known that the effective photo-elastic constant p_{eff} is given by

$$p_{eff} = \vec{e}_1 (p\gamma) \vec{e}_0 = 0.5 (p_{11} - p_{12}) \approx 0.055, \tag{20}$$

where the vectors $\vec{e}_0$ and $\vec{e}_1$ describe the polarization states of incident and scattered light beams, respectively. Within the anomalous non-collinear acousto-optical interaction, the eigen polarization vectors $\vec{e}_0$ and $\vec{e}_1$ of the incident and scattered light beams should be orthogonal to one another $\vec{e}_0 \perp \vec{e}_1$, and they both have to be lying in the same plane as the wave vector $\vec{K} \| [110]$. For the sake of simplicity, in this case, one can take $\vec{e}_0 \| \vec{K}$ and $\vec{e}_1 \| \vec{u}$, i.e. $\vec{e}_0 = (1,1,0)/\sqrt{2}$ and $\vec{e}_1 = (1,-1,0)/\sqrt{2}$. Then, the magnitude of $M_2 = n_O^3 \, n_E^3 \, (p_{eff})^2 / (\rho \, V^3)$ includes also the material density $\rho = 7.2$ g/cm^3 and a pair of rather dispersive refractive indices n_O and n_E. The last two parameters should be taken exactly at the wavelength λ exploited under condition that the correct tilt angle ψ is taken into account, see Table 2. These values of M_2 demonstrate that the anomalous light scattering, governed by the pure slow shear acoustic mode in the calomel are sufficiently efficient and this crystal is able to provide effective two-phonon light scattering.

Then, the above-chosen first maxima in light distribution require the following optimized power parameters $(\sigma x)_{1,Opt} = 2.785$, 2.965 and 3.200 at $f_0 \approx 57.8$, 71.0 and 82.6 MHz when $\alpha = 0.8851$, 0.1336, 0.1808 cm^{-1} and the correction factor of apodization $\kappa \approx 1.019$, 1.043, 1.080, respectively. With $x \equiv L$ and $L = 0.2$ cm, one can find $\sigma_{1,Opt} = 13.925$, 14.825, and 16.000 cm^{-1}. Now, the standard determination for σ [22] with $\cos\theta \approx 1$ can be re-written specifically to the acoustic power density P_1 needed for the first maxima as

$$P_1 \approx \frac{2\lambda^2 \sigma_{1Opt}^2}{\pi^2 M_2}. \tag{21}$$

Thus, for example at $\lambda = 405$ nm and $f_0 \approx 82.6$ MHz, Eq.(21) gives the optimized value of $P_1 \approx 103$ mW/mm^2, see Table 2. Additionally, one has to find the Bragg angles of light incidence for the two-phonon regime as $\theta \approx K / k = f_0 \lambda / V$.

Table 2. Pre-experimental estimations; here, $d_S = \kappa \lambda F / D$ is an ideal spot size in the approximation of geometric optics with the correction factor of apodization $\kappa \approx 1.019$, 1.043, and 1.080, F = 85 cm, and D = 5.2 cm.

λ, nm	**f_0, MHz**	**ψ, rad**	**n_O**	**n_E**	**θ, rad**	**d_S, μm**	**M_2, s^3/ g**	**P_1, mW/mm^2**
405	57.8	0.044	2.0826	2.0837	0.068	6.746	821.7×10^{-18}	78
	71.0	0.055	2.0826	2.0843	0.083	6.905	822.4×10^{-18}	89
	82.6	0.064	2.0826	2.0848	0.096	7.149	823.1×10^{-18}	103
633	57.8	0.081	1.9634	1.9662	0.105	10.543	578.5×10^{-18}	272
	71.0	0.100	1,9634	1.9677	0.129	10.792	$579{,}8 \times 10^{-18}$	307
	82.6	0.116	1.9634	1.9692	0.151	11.175	581.1×10^{-18}	358

6 PROOF-OF-PRINCIPAL EXPERIMENTAL DATA

6.1. Experiment arrangement

First, one can estimate the potential contributions of the acoustic losses for the chosen slow shear elastic mode passing along the [110]-axis, whose displacement vector is oriented along the $[1\bar{1}0]$-axis. Because of the coefficient of linear attenuation is $\Gamma \approx 230$ dB/(cm GHz^2) in a calomel single crystal [5], the factor α [cm^{-1}] of the amplitude acoustic losses is determined as α [cm^{-1}] = 0.1152 Γ [dB/(cm GHz^2)] f ^{2}[GHz]. The carrier frequencies $f_0 \approx$ 57.8, 71.0, and 82.6 MHz at the light wavelengths 405 and 633 nm, peculiar to the non-collinear two-phonon light scattering in calomel, had been chosen above. Consequently, one can estimate the amplitude factors for linear acoustic losses by γ [dB/cm] = Γf_0^2, which gives γ = 0.0768 dB / cm, α = 0.08875 cm^{-1}; γ = 0.1160 dB / cm, α = 0.1336 cm^{-1}; and γ = 1.56 dB / cm; α = 0.18125 cm^{-1}, respectively, for those frequencies.

Additionally, one has to take into account the losses needed for converting the input electronic signal into an acoustic one, which are usually slightly exceeding 2 dB. However within these our experiments, we had decided to modify the piezoelectric transducer. The practically important problem is connected with relatively narrow frequency and spectral bandwidth of the AOC exploiting the non-collinear two-phonon light scattering. The matter is that calomel is sufficiently effective acousto-optical material, so that the bandshape width of the calomel-made AOC can be expanded at the cost of decreasing the efficiency of that AOC. In so doing, the thickness of upper electrode, placed over piezoelectric material, had been a little bit increased to implement the effect of oscillation damping. The goal of such a low damping was to decrease the quality factor of acoustic resonance inherent in that piezoelectric transducer. Our experimental estimations have demonstrated that such a damping grew the losses for converting the electronic signal into an acoustic one up to 3.0 – 3.5 dB, while the acoustic resonance curve of that piezoelectric transducer showed a broader maximum.

Previously, we had to restrict ourselves by a maximum level $P \leq 0.5$ W/mm^2 of acoustic power density. However, a design of the damped piezoelectric transducer admits the acoustic power density by a magnitude of about $P_1 \leq 3.5$ W/mm^2 for the acoustic beam cross section of about 4 mm^2 in the AOC under consideration. The produced estimations demonstrate that the above-required levels of the parameters P_1 and $\sigma_{1,Opt}$ for the first unit-level maxima lie in the ranges of accessible values. One can find from Eq.(21) that reaching the next maxima [10] need much higher acoustic power densities in comparison with the first ones. This looks rather conjectural from the viewpoint of requirements for the electric strength inherent in the available piezoelectric transducer. After that, pre-experimental estimations for the calomel-made AOC with D = 5.2 cm and $L_{min} \approx 0.2$ cm can be summarized in Table 3. These estimations imply exploiting the pure slow shear elastic mode with the acoustic velocity V = 0.347×10^5 cm/s in the scheme of the standard acousto-optical spectrum analyzer with the integrating lens of the focal distance F = 85 cm.

The design of the calomel crystalline AOC under consideration, operating in the regime of the non-collinear two-phonon light scattering, is presented in detail in Fig. 10. The piezoelectric transducer represented by a thin plate made of the 163º Y-cut $LiNbO_3$ single crystal had been placed on the (110) crystallographic plane of the calomel crystal. It provided the excitation of a slow-shear mode acoustic beam with the cross section of about 4 mm^2 and the length L = 0.2 cm of interaction in calomel. The needed Bragg and tilt angles, whose orientations are depicted in Fig. 10, are enumerated in Table 2.

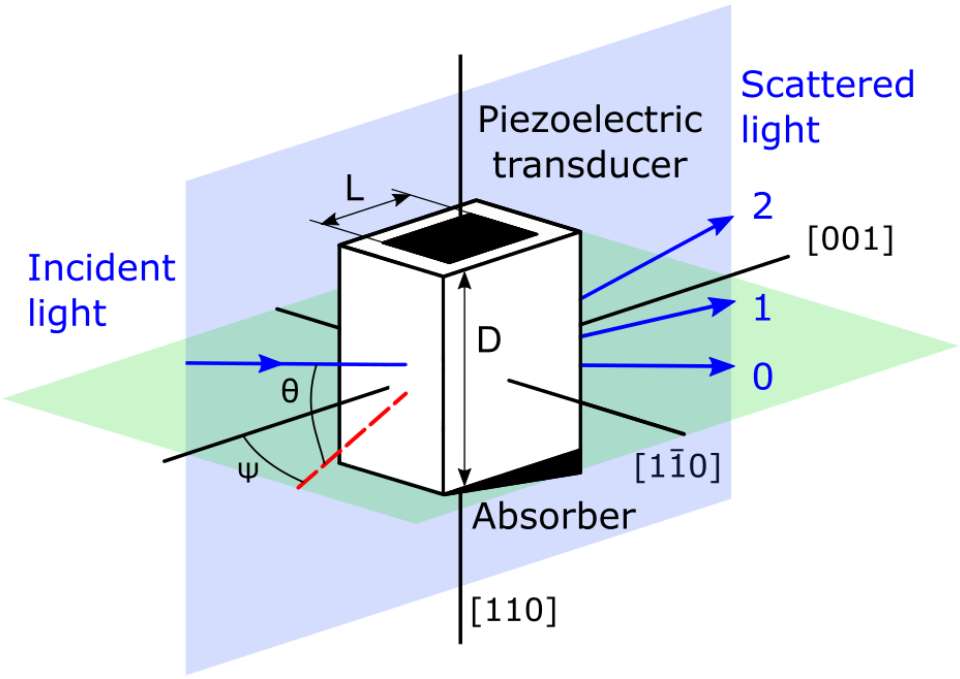

Fig. 10. The design of the calomel AOC.

6.2. Experimental results

Our proof-of-principal experiments had been performed with a wide-aperture Bragg AOC based on the unique calomel (α-Hg_2Cl_2) single crystal, which had an active optical aperture of about 52×2 mm, see Fig. 10. This pioneer AOC allowed a maximum input acoustic power of about 20 W. It was able to operate over all the visible range starting from the optical wavelength λ = 405 nm, which combines the convenience of operating in just the visible range with the best-expected performances inherent in this AOC. Practically, we used optical wavelengths λ = 405 and 633 nm from the single frequency solid-state lasers CL-405-050-S and DL-633-050-S (CrystaLaser). The CW-light radiation had linear state of the incident light polarization oriented almost along the crystallographic axis [110] of that AOC. First, the calomel-based AOC was prepared to be governed by the radio-wave signals at the central frequency $f_0 \approx 57.8$ MHz and then, after re-polishing and re-arranging the piezoelectric transducer, at the central frequencies $f_0 \approx 71.0$ and 82.6 MHz. A set of electronic equipment for both generating and registering the corresponding electric ultra-high-frequency (UHF) radio-wave signals had been exploited. Initially, the tunable UHF-signal was applied to the electronic input port of the AOC through a wide-band UHF-amplifier HD19152 (0.15 – 230 MHz, 20 W) and the corresponding impedance-matching electronic circuits, see Fig. 11.

The optical part of our experiments included a 15-mm Glan-Taylor linear polarizer (the extinction ratio ~10^5, Thorlabs) and a four-prism (Edmund Optics) beam expander, which operated with the coherent light beams polarized in the plane of expanding and provided rather flat (non-uniformities were better than ~ 10%) optical beam profiles. During the experiments with the beam shaper rather accurate angular adjusting of the incident light beams had been achieved. By this it means that both the correct Bragg angles of incidence and the needed tilt angles had been optimized. The 3-inch achromatic doublet lens (Edmund Optics) with the focal length of about 85 cm had been used as the integrating lens, and the multi-pixel CCD-linear array (Toshiba) consisting of 4.7 μm pixels was playing the role of a photo-detector. The layout of the experimental set-up is presented in Fig. 5, where only the 2-nd order of light scattering pattern is shown.

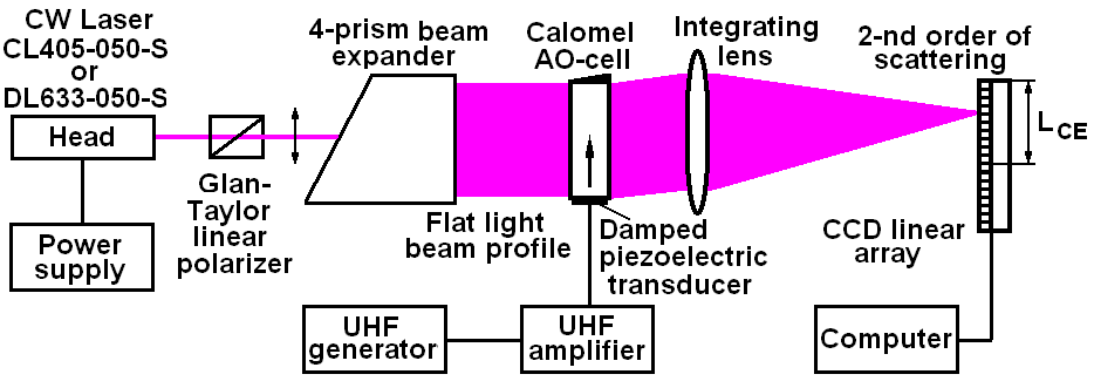

Fig. 11. A layout of the experimental set-up; only the 2-nd order of light scattering is depicted.

The experiments consisted of two parts. The first of them included detecting the frequency bandshape with a low oscillation damping, i.e. determining the effective bandwidth of the Bragg non-collinear two-phonon light scattering at a 0.405–level of light intensity. The second part of those experiments was related to estimating possible spectral resolution within involving this AOC into the optical spectrum analysis. It was done via measurements of individual resolvable spots in the focal plane of the integrating lens for the light deflected by into the second order of scattering. Figure 12 shows an example of the experimental trace for the frequency bandshape inherent in the calomel AOC with the damped piezoelectric transducer at the central frequency about 82.6 MHz, which had been detected under lighting by the coherent violet light λ = 405 nm. The total experimental frequency bandwidth at a 0.405–level of light intensity has been estimated by $\Delta f_M \approx$ 2.856 MHz. Precise optical measurements had been performed at two wavelengths 405 and 633 nm to obtain sufficiently reliable estimations for the frequency resolution provided by the calomel AOC together with the above-described optical system, including the CCD linear array. The performed measurements had been done in the regime of the so-called "hot cell", i.e. with a radio-wave signal applied at the input port of the α-Hg_2Cl_2–cell. Figure 13 depicts the intensity profile with the spot size of about 8.3 microns with the side lobe level of about 6.6 %, which include affecting the light distribution in a spot by the acoustic losses of 8 dB / aperture. The measurements showed that the main lobe of a spot gave lighting about two pixels of the CCD-row that provided acceptable resolution of a pattern from viewpoint of the sampling theorem.

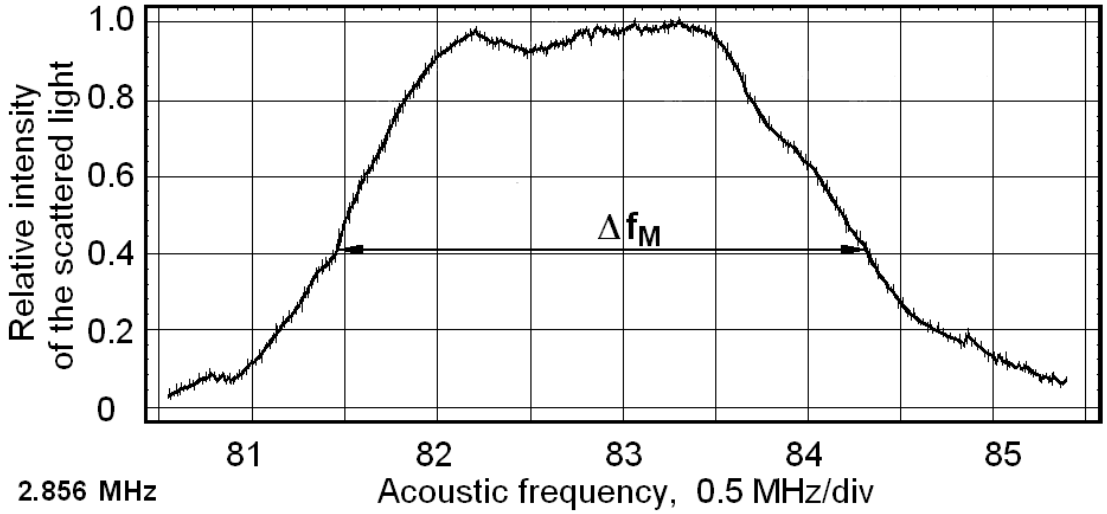

Fig. 12. Experimentally obtained frequency bandshape of the calomel-made AOC at $f_0 \approx$ 82.6 MHz and λ = 405 nm.

As it had been noted, our experimental results have been obtained using the integrating lens with F = 85 cm at the wavelength 405 nm, so that theoretically the spot size is $d_S = \kappa \lambda F / D \approx 7.149$ μm. Together with this, the plot in Fig. 13 exhibits the experimental spot size $d_M = \kappa \lambda F / D_M \approx 8.3$ μm that corresponds to the effective aperture $D_M \approx 4.151$ cm for the AOC.

The calomel crystal has rather high refractive indices. For example, the main ones are about $N_O = 2.083$ and $N_E = 3.038$ at $\lambda = 405$ nm used during the experiments. This is why one can expect significant optical attenuation inside the crystal and remarkable reflections from the facets of calomel-based AOC. Undoubtedly, to minimize potential optical losses the facets of similar AOC ought to have anti-reflection coating as it had been noted in the introduction. Nevertheless, we had performed our proof-of-principle experiments with the AOC that had not been coated. Therefore, the relative efficiency of light scattering into the second order had been first experimentally estimated and then measured at the output facet of the AOC. In so doing, the light intensity detected at the output facet, transmitted through the cell in the absence of an external UHF electronic excitation, had been counted as the unity. The light intensity scattered into the second order in the presence of that electronic signal and measured at the output facet had been considered as the usable optical signal caused by UHF electronic signal. The ratio of this usable optical signal to the initially transmitted light intensity (both are measured at the output facet of that AOC), one can consider as the relative efficiency of light scattering. Thus the relative efficiency, determined as it has been described above, had been measured at the optimal acoustic frequencies about $f_0 \approx 57.8$, 71.0**,** and 82.6 MHz as well as at $\lambda = 405$ and 633 nm. The maximum relative efficiency at the optimal acoustic frequency about 82.6 MHz and $\lambda = 405$ nm had been experimentally estimated by the value ~ 0.93.

Figure 13 demonstrates the light intensity profile of a resolvable spot, which is a result of the standard processing provided by computer software accompanying the CCD-camera. One can see in Fig. 13 that full width at a 0.405-level of maximum of the main lobe can be estimated by about of 8.3 microns.

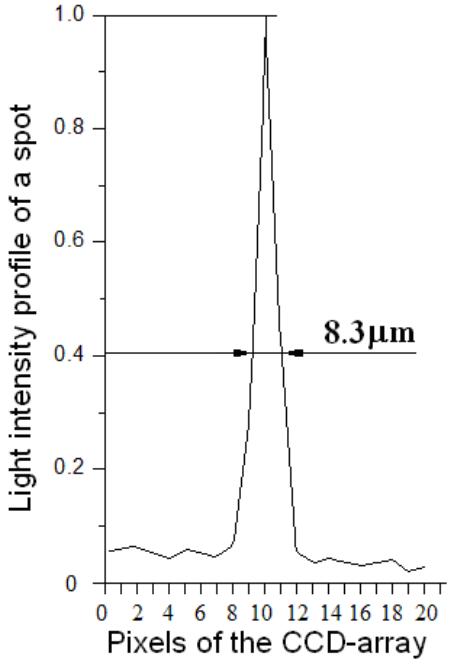

Fig. 13 Light intensity profile of an individual resolvable spot for the calomel-based AOC at $\lambda = 405$ nm.

The last data show that about 20% of the active optical aperture of the AOC is lost due to imperfectness of the lens and AOC's crystalline material together with the total effect of linear acoustic losses B = 8 dB per aperture. Therefore, instead of theoretical limit of the frequency resolution $\delta f_{Th} = V / 2D \approx 3.337$ kHz, one yields the measured value $\delta f_M = V / 2D_M \approx 4.18$ kHz, which leads to the experimentally obtained spectral resolution $\delta\lambda_M = \lambda\, \delta f_M / f_0 \approx 0.205$ Å. at $\lambda = 405$ nm. Then, $\Delta\lambda_M = \Delta f_M\, \lambda / f_0 \approx 140.0$ Å (instead of the theoretical value $\Delta\lambda_{Th} \approx 104.47$ Å because of damping the piezoelectric transducer). Thus the experimentally obtained number of resolvable spots is $N_M = \Delta f_M / \delta f_M = \Delta\lambda_M / \delta\lambda_M \approx 683$ spots.

In Table 3, the comparison of theoretical and experimental results is presented. One can see that some experimentally obtained data, namely, the frequency and spectral bandwidths as well as the numbers of resolvable spots exhibit general tendency to exceed the above-calculated theoretical values. This tendency takes place despite the presence of natural imperfectness peculiar to all the optical components in our experimental set-up. Similar results can be attributed to the use of damping the piezoelectric transducers in the developed AOC.

Table 3. Comparison of theoretical and experimental data; $\delta f_{Th} \approx 3.337$ kHz and $\delta f_M \approx 4.18$ kHz.

λ, nm	**f_0, MHz**	**Δf_{Th}, MHz**	**Δf_M, MHz**	**$\Delta\lambda_{Th}$, Å**	**$\Delta\lambda_M$, Å**	**$\delta\lambda_{Th}$, Å**	**$\delta\lambda_M$, Å**	**N_{Th}**	**N_M**
405	57.8	3.045	4.129	213.36	289.3	0.23375	0.2929	913	988
405	71.0	2.479	3.290	141.40	187.6	0.19035	0.2384	743	787
405	82.6	2.131	2.856	104.47	140.0	0.16357	0.2049	639	683
633	57.8	1.837	2.605	201.15	285.3	0.36533	0.4578	571	623
633	71.0	1.495	2.084	133.31	185.8	0.29751	0.3727	448	498
633	82.6	1.285	1.796	98.49	137.6	0.25557	0.3203	385	430

Finally, the maximal expected lighted length in the focal plane of the integrating lens is $L_{CE} = d_M N_M < 9.0$ mm, i.e. capabilities of the experimental optical system lie in the frames of the exploited multi-pixel CCD-array. The obtained results with the developed calomel AOC (the spectral resolution $\delta\lambda_M \approx 0.205$ Å at 405 nm, which gives the resolving power exceeding $R_M = 19{,}800$ with the spectral bandwidth $\Delta\lambda_M \approx 140.0$ Å) have a gain compared with the most advanced to our knowledge, acousto-optical spectrometers for space or airborne operations of the twenty-first century [23-25]. Furthermore, one can take the other data from the recently obtained results [10] with calomel AOF (the spectral resolution was $\delta\lambda \approx 0.235$ Å at 405 nm, which gives the resolving power $R \approx 17{,}200$). By this it means that our new experimental result for the above-described calomel AOC (with the increased operation frequency and higher acceptable acoustic losses per optical aperture) can be considered as the best one can mention at the moment.

7 CONCLUSION

The main potentials of a new wide-aperture crystalline calomel-made AOC have been investigated. This AOC operates in an advanced nonlinear regime of the non-collinear two-phonon light scattering, so that the cell's characterization is a non-trivial procedure. The novelty consists also in the fact that principally new features, revealed recently in that phenomenon of scattering [10], have been essentially incorporated into the design of that AOC to be studied more accurately and thoroughly. The easiest way for the mentioned important features come to light in tetragonal crystals, like the calomel crystal, which is able to display the acousto-optical nonlinearity governed by the acoustic waves of finite amplitude. Moreover, such square-law parametric nonlinearity exhibits itself under the action of moderate acoustic power density in calomel crystal having in addition to that the linear acoustic attenuation. Strongly nonlinear behavior of the transmitted light intensity and the angular-frequency mismatch in the AOC lead to a sequence of the local unit-level maxima and a variety of the transfer function profiles into the second order of the scattered light. At the current stage of studies, the first unit-level maximum, which is specific to the nonlinear transfer function of this AOC and appears at not too high acoustic power density, had been chosen for investigations in detail. The first unit-level maximum looks attractive when the calomel-made AOC is exploited practically for the precise spectrum analysis of optical signals due to an opportunity to shape a moderate apodization using that nonlinearity.

The formerly uncovered complementary physical degree of freedom, inherent in similar advanced nonlinear regime of two-phonon light scattering, had been built into that calomel-made AOC as well. It had been done with the aims to vary the central acoustic frequency and to hold the desired possibility to doubling the spectral resolution through the application of two-phonon processes. Therefore, one can say that the calomel-made AOC has been progressed for the goals of optical spectrum analysis with an essentially improved spectral resolution. Usually, a remarkable acoustic attenuation in crystalline materials is significant limiting factor, which reduces potential performances of AOCs and acousto-optical spectrum analysis as well. To investigate this aspect, three levels of the linear acoustical losses, namely 4, 6**,** and 8 dB per optical aperture of the calomel-made AOC, had been incorporated in our analysis and experimental investigations to eliminate artificially overestimated additional limitations at the today's state-of-art studies. The required calculations had been fulfilled to develop a unique wide-aperture calomel-made AOC and exploit it during the experiments at three central acoustic frequencies 57.8, 71.0**,** and 82.6 MHz as well as at two different optical wavelengths $\lambda = 405$ and 633 nm with optical aperture $D = 5.2$ cm of that AOC. Three central acoustic frequencies 57.8, 71.0**,** and 82.6 MHz lead to three levels of acoustic attenuation $B = 4$, 6, and $B = 8$ dB per that aperture due to cell's excitation by the slow shear acoustic mode passing along the [110]-axis. For this purpose, specific trajectories of light beams inside the calomel crystal of that AOC had been selected for the implementation of the non-collinear two-phonon light scattering by acoustic waves of finite amplitude. The chosen trajectories were able to satisfy the phase synchronism for this nonlinear process at the above-noted frequencies with maximal efficiency and spectral bandwidth. Additionally, well-known high acousto-optical efficiency of calomel crystal had been practically exploited to extend the AOC's spectral bandwidth at the sacrifice of its efficiency. As a result, we have performed a set of proof-of-principle experiments with the developed pioneer AOCs based on very effective acousto-optical material, i.e. on the calomel (α-Hg_2Cl_2) crystal. The obtained experimental data mainly confirm the above-progressed analytical and numerical estimations related to variations of the acoustic frequencies and acoustic losses. The achieved spectral resolution 0.205 Å at 405 nm and the resolving power 19,800 are the best to our knowledge for acousto-optical spectrometers dedicated to space or airborne operations.

These results are significant due to the progress achieved in the spectral resolution of an acousto-optical spectrometer, which would enhance the measurements in several scientific areas. For instance, this resolution exceeds all the previous AO spectrometers in the literature [23-25]. Considering the use of this new technique would give us the option to quantify the abundances of different elements, less affected by line blending, such as Li, Fe, O, or Na [26], for example. Finally, one can conclude that these results can be considered as the real progress in designing a new type of the AOCs oriented to innovative technique in an advanced optical spectrum analysis with the significantly enhanced spectral resolution.

ACKNOWLEDGMENTS

The work was supported by CONACyT, project # 61237 (initially) and AdlOptica GmbH (Berlin, Germany).

REFERENCES

1. J. A. Kusters, D. A. Wilson, and D. L. Hammond, "Optimum crystal orientation for acoustically tuned optical filters", J. Opt. Soc. Am. 64 (4), 434-440, (1974).
2. A. S. Shcherbakov, A. O. Arellanes, and E. Bertone, “Advanced collinear $LiNbO_3$ acousto-optical filter for astrophysical spectroscopy in the near-ultraviolet: exploring high-spectral resolution”, J. Astron. Telesc. Instrum. Syst. 1(4), 045002 (2015) and references within this article.
3. N. Uchida and N. Niizeki, "Acoustooptic deflection materials and techniques", Proc. IEEE 61 (8), 1073-1092, (1973).
4. M. Gottlieb, A. P. Goutzoulis, and N. B. Singh, "Fabrication and characterization of mercurous chloride acoustooptic devices", Appl. Opt. 26, 4681–7 (1987).
5. M. P. Shaskolskaya, Acoustic Crystals, Moscow, (Nauka, 1982).
6. J. S. Kim; S. B. Trivedi; J. Soos; N. Gupta; W. Palosz; "Development of mercurous halide crystals for acousto-optic devices", Proc. SPIE 6661, Imaging Spectrometry XII, 66610B (2007).
7. N. Gupta, "Investigation of a mercurous chloride acousto-optic cell based on longitudinal acoustic mode", Appl. Opt. 48, C151 (2009). http://dx.doi.org/10.1364/AO.48.00C151
8. R. Maksimenka, et al., "Direct mid-infrared femtosecond pulse shaping with a calomel acousto-optic programmable dispersive filter", Opt. Lett. 35, 3565-3567 (2010).
9. N. B. Singh; et al., "Acousto-optical imagers for chemical and biological detection: growth and characterization of Hg2Cl2-xBrx crystals", Proc. SPIE 8719, Smart Biomedical and Physiological Sensor Technology X, 87190V (2013).
10. A. S. Shcherbakov and A. O. Arellanes, "Advanced regime of the noncollinear two-phonon acousto-optical interaction governed by elastic waves of finite amplitude and optical spectrum analysis", J. Opt. Soc. Am. B 32, 1930-1940 (2015)
11. G. Lu and B. Fei, “Medical hyperspectral imaging: a review”, J. Biomed. Opt. 19 (1), 010901 (2014).
12. W. Zima, “Spectroscopic observations for asteroseismology”, J. Phys.: Conf. Ser. 118 (1), 012014 (2008).
13. C. Aerts, J. Christensen-Dalsgaard, and D. W. Kurtz, “Asteroseismology, Astronomy and Astrophysics”, Springer Science+Business Media B.V (2010).
14. J. K. Zhao et al., “70 DA white dwarfs identified in LAMOST pilot survey”, The Astronomical Journal 145 140G (2013).
15. A. Korpel. *Acousto-Optics*, 2nd Ed., N.-Y., (Marcel Dekker, 1997).

16. R. W. Damon, W. T. Maloney, D. H. McMahon, "Interaction of light with ultrasound: phenomena and applications," in Physical Acoustics: Principles and Methods, W. P. Mason, R. N. Thurston, eds., Vol. VII, pp. 273–366, New York (Academic Press, 1970).
17. M. Born, E. Wolf, *Principles of Optics*, Cambridge, UK, (Cambridge Univ. Press, 1999).
18. V. I. Balakshy, V.N. Parygin, and L.I. Chirkov. Physical Principles of Acousto-Optics, Radio I Svyaz, Moscow, (1985).
19. H. Schmitzer, H. Wagner, W. Dultz, and M. Kühnelt, "Phase-matched third-harmonic generation in mercury-(I)-chloride", Appl. Opt. 41 (3), 470-474 (2002).
20. W. R. Klein and B. D. Cook, "Unified approach to ultrasonic light diffraction", IEEE Trans. Sonics & Ultrasonics, SU-14, 123 - 134 (1967).
21. A. P. Sukhorukov, Nonlinear Wave Interactions in Optics and Radiophysics, (Nauka, Moscow, 1988).
22. S. Shcherbakov, A. O. Arellanes, and S. A. Nemov, "Transmission function collinear acousto-optical interaction occurred by acoustic waves of finite amplitude", J. Opt. Soc. Am. B 30 (12), 3174-3183, (2013).
23. V. Y. Molchanov et al., "An acousto-optical imaging spectrophotometer for astrophysical observations," Astron. Lett. 28, 713–720 (2002).
24. O. Korablev, J. L. Bertaux, A. Grigoriev et al., "An AOTF-based spectrometer for the studies of Mars atmosphere for Mars Express mission," Adv. Space Res. 29, 143–150 (2002).
25. O. Korablev, A Fedorova, J. L. Bertaux et al., "SPICAV IR acousto-optic spectrometer experiment on Venus Express," Planet. Space Sci. 65, 38–57 (2012).
26. T. Hsyu et al., "Light-Element Chemistry and the Double Red Giant Branch in the Galactic Globular Cluster NGC 288", Publications of the Astronomical Society of the Pacific 126 (941), 597-604 (2014).